Journal of Biomolecular NMR (2019) 73:141–153
https://doi.org/10.1007/s10858-019-00237-5

ARTICLE

Hybridization of TEDOR and NCX MAS solid-state NMR experiments for simultaneous acquisition of heteronuclear correlation spectra and distance measurements

T. Gopinath[1] · Songlin Wang[1] · John Lee[1] · Hideki Aihara[1] · Gianluigi Veglia[1,2]

Received: 19 December 2018 / Accepted: 12 February 2019 / Published online: 25 February 2019

Abstract
Magic angle spinning (MAS) solid-state NMR (ssNMR) spectroscopy is a major technique for the characterization of the structural dynamics of biopolymers at atomic resolution. However, the intrinsic low sensitivity of this technique poses significant limitations to its routine application in structural biology. Here we achieve substantial savings in experimental time using a new subclass of Polarization Optimized Experiments (POEs) that concatenate TEDOR and SPECIFIC-CP transfers into a single pulse sequence. Specifically, we designed new 2D and 3D experiments (2D TEDOR-NCX, 3D TEDOR-NCOCX, and 3D TEDOR-NCACX) to obtain distance measurements and heteronuclear chemical shift correlations for resonance assignments using only one experiment. We successfully tested these experiments on *N*-Acetyl-Val-Leu dipeptide, microcrystalline U-^{13}C,^{15}N ubiquitin, and single- and multi-span membrane proteins reconstituted in lipid membranes. These pulse sequences can be implemented on any ssNMR spectrometer equipped with standard solid-state hardware using only one receiver. Since these new POEs speed up data acquisition considerably, we anticipate their broad application to fibrillar, microcrystalline, and membrane-bound proteins.

Keywords Solid-state NMR · Magic angle spinning · Polarization optimized experiments · TEDOR · SPECIFIC-CP · NCA · NCO · DARR · Microcrystalline proteins · Membrane proteins · Sarcolipin · Succinate–acetate permease protein

Introduction

Magic angle spinning (MAS) solid-state NMR (ssNMR) spectroscopy plays a central role in the characterization of structures, motions, and interactions of biological macromolecules such as fibrillar, microcrystalline, and membrane proteins (Ader et al. 2009; Castellani et al. 2002; Gustavsson et al. 2013; Hong et al. 2012; Hu et al. 2010; Wang and Ladizhansky 2014). Sensitivity and resolution, however, still limit its routine application to membrane proteins, where motion and sample heterogeneity complicate the interpretation of NMR spectra. In addition to this, the high lipid-to-protein ratios essential to maintain the functional integrity of membrane proteins also dilute the protein content of MAS samples and substantially increase the experimental time necessary to obtain high-quality spectra. As a result, NMR of membrane proteins requires longer acquisition times compared to fibrils or microcrystalline protein preparations.

To overcome these challenges and reduce experimental time, we developed Polarization Optimized Experiments (POEs), a class of pulse sequences that make the best out of nuclear polarization (Gopinath and Veglia 2012a, b, 2013, 2018). POEs are ideal for MAS experiments on U-^{13}C,^{15}N labeled biomolecules at low-to-moderate spinning rates, which are often crucial to preserve enzymatic function (Gustavsson et al. 2013). POEs enable the acquisition of multiple 2D and 3D NMR spectra simultaneously in a single experiment, resulting in a substantial saving of experimental time. A key element of POEs is the simultaneous cross-polarization (SIM-CP) scheme that matches Hartmann-Hahn conditions for ^{1}H, ^{13}C, and ^{15}N contemporarily to generate an additional ^{15}N polarization (N_z) that remains stored along the

✉ Gianluigi Veglia
vegli001@umn.edu

[1] Department of Biochemistry, Molecular Biology, and Biophysics, University of Minnesota, 6-155 Jackson Hall, Minneapolis, MN 55455, USA

[2] Department of Chemistry, University of Minnesota, Minneapolis, MN 55455, USA

z-axis for several milliseconds due to its relatively long longitudinal relaxation time (T_1) (Gopinath and Veglia 2012a, b). Therefore, after the main experiment is recorded (first acquisition), the N_z polarization is utilized to generate one or more *n*D spectra within the same pulse program (Gopinath and Veglia 2012, 2013). Analogously, ^{13}C polarization generated by SIM-CP can be stored along the z-axis (C_z) and utilized for multiple experiments as previously demonstrated (Gopinath and Veglia 2012a, b, 2016). The FIDs originating from POEs are usually saved in different memory allocations and processed into separate spectra (Gopinath and Veglia 2012a, b, 2018). The straightforward implementation on commercial NMR spectrometers equipped with only one receiver and probes for bio-solids (Low-E or E-free) made POEs appealing to the broader NMR community (Gor'kov et al. 2007; McNeill et al. 2009; Stringer et al. 2005). In fact, other groups extended POE to ^{1}H detected experiments to obtain a considerable gain in sensitivity and time efficiency (Bellstedt et al. 2012; Das and Opella 2016; Sharma et al. 2016).

Our original POEs were designed to record a ^{13}C–^{13}C homonuclear correlation spectrum as the main experiment, followed by single or multiple ^{13}C–^{15}N correlation spectra in subsequent acquisitions. Here, we expanded the POE toolkit (Gopinath et al. 2016) by hybridizing transferred echo double resonance (TEDOR) (Jaroniec et al. 2002; Rienstra et al. 2002; Hong and Griffin 1998; Andrew et al. 1992) and spectrally induced filtering in combination with cross-polarization (SPECIFIC-CP) (Baldus et al. 1998) transfer elements to record ^{13}C–^{15}N correlation experiments in the first and subsequence multiple acquisitions. With these hybridized pulse sequences, we were able to combine distance measurements and heteronuclear chemical shift correlation experiments. We successfully performed these experiments on U-^{13}C,^{15}N microcrystalline ubiquitin as well as two U-^{13}C,^{15}N labeled membrane proteins: sarcolipin (SLN), a single-pass transmembrane protein (Traaseth et al. 2008), and succinate–acetate permease (SatP), with six transmembrane helices (Sa-Pessoa et al. 2013; Sun et al. 2018; Qiu et al. 2018).

Materials and methods

The expression, purification, and microcrystalline preparation of recombinant U-^{13}C,^{15}N ubiquitin were carried out as reported by Igumenova et al. (2004). Recombinant SLN was expressed in *E. coli* bacteria using minimal M9 media enriched with ^{13}C glucose (Sigma) and ^{15}N ammonium chloride (Sigma) as reported previously (Buck et al. 2003). Succinate–acetate permease (SatP) was expressed and purified from *E. coli* bacteria as a SUMO fusion protein. Briefly, *E. coli* SatP was cloned into a pE-SUMOpro-Amp (LifeSensors) vector and expressed in *E. coli* BL21(DE3) cells. Cells were grown to an optical density (OD) at 600 nm of 1.0 at 37 °C in M9 media with 50 mg/L ampicillin then induced with 1 mM isopropyl-D-thiogalactoside (IPTG). All purifications were carried out on ice. Cells from 2 L of culture were harvested and lysed by sonication in 50 mM Tris buffer (pH 7.4), 500 mM NaCl, and 0.5 mM phenylmethylsulforyl fluoride (PMSF). SatP was solubilized from whole lysed cells in 50 mM Tris buffer (pH 7.4), 500 mM NaCl, 10% glycerol, and 200 mM Octyl Glucoside (OG, Anatrace) or 10 mM Octyl Glucose Neopentyl Glycol (OGNG, Anatrace) for 2 h at 4 °C. After centrifugation at 60,000×*g*, solubilized SatP protein in the supernatant was batch-bound to Ni-NTA resin (Qiagen) for 1 h, washed with 25 bed volumes of 50 mM Tris buffer (pH 7.4), 300 mM NaCl, 10% glycerol, 40 mM OG, and 40 mM imidazole, then eluted with 250 mM Tris buffer (pH 7.4), 300 mM NaCl, 10% glycerol, 40 mM OG, and 300 mM imidazole. Imidazole was removed using a BioRad Econo-Pac 10DG desalting column and the histidine-tagged SUMO was removed by digestion with histidine-tagged SUMO protease for 12 h at 4 °C. The protein sample was batch bound to Ni-NTA resin and the flow through containing SatP was concentrated and further purified on a GE Superdex 200 gel filtration column with a mobile phase of 50 mM Tris buffer (pH 7.4), 100 mM NaCl, 10% glycerol, and 40 mM OG.

For NMR experiments, approximately 0.6 mg of SLN or 8 mg SatP were reconstituted into 12 mg of 1,2-dimyristoyl-sn-glycero-3-phosphocholine (DMPC, Avanti Polar Lipids) at lipid-to-protein ratios of 100 and 40, respectively (Gustavsson et al. 2013). All the experiments were implemented on Agilent and Bruker spectrometers operating at a ^{1}H Larmor frequency of 600 MHz. Experiments on U-^{13}C,^{15}N SLN, U-^{13}C,^{15}N ubiquitin, and U-^{13}C,^{15}N NAVL dipeptide were acquired using a 3.2 mm scroll coil MAS probe with 25 µL sample volume. Spectra of U-^{13}C,^{15}N SatP were acquired using a 1.3 mm Bruker MAS probe with 4 µL sample volume. All data were acquired with a recycle delay of 3 s and MAS rate (ν_r) set to 12.5 kHz, which corresponds to an 80 µs rotor period (τ_r). The maximum RF amplitude on the ^{1}H channel was set to 100 kHz, which corresponds to a 90° pulse of 2.5 µs; whereas the RF amplitude for the ^{13}C and ^{15}N channels was set to 41.6 kHz and corresponds to a 90° pulse of 6 µs. During the REDOR period (Hing and Schaefer 1993; Gullion and Schaefer 1989), 180° pulses of 12 µs were applied on both ^{13}C and ^{15}N channels. The 180° pulses on the ^{15}N channel were phase cycled using the XY-4 scheme (Gullion et al. 1990). CP and SIM-CP contact times were set to 500 µs, during which the RF amplitudes of ^{13}C and ^{15}N were set to 35 kHz, and the ^{1}H RF amplitude was ramped from 90 to 100%, with the center of the ramp set to 60 kHz. During

TEDOR mixing, t_1 evolution, and t_2 acquisition periods, a SPINAL-64 ^{1}H decoupling sequence was used on the ^{1}H channel with 100 kHz RF amplitude (Fung et al. 2000). The t_2 acquisition times for ^{13}C detection were set to 15 ms with 10 µs dwell time; whereas the ^{15}N signal was evolved during t_1 with 320 µs (equal to $4\times\tau_r$) dwell time for 32 increments, corresponding to a maximum t_1 evolution time of 10.24 ms. For the U-^{13}C,^{15}N NAVL sample, 16 increments of t_1 were acquired with a dwell time of 640 µs. The SPECIFIC-CP transfer between ^{15}N and ^{13}Cα or ^{13}CO was achieved using a tangent-shaped ramp pulse on ^{13}C and a constant amplitude pulse applied on ^{15}N, with CW (continuous wave) decoupling applied on ^{1}H nuclei using 100 kHz RF amplitude. The offset for ^{13}C was set to 50 and 175 ppm for NCA and NCO transfer periods, respectively. The RF amplitudes of ^{13}C were set to 18.75 kHz ($1.5\times\nu_r$) and 43.75 kHz ($3.5\times\nu_r$) for NCA and NCO transfers, respectively, whereas the ^{15}N RF amplitude was arrayed around 31.25 kHz ($2.5\times\nu_r$) to obtain the maximum intensity of signals (Franks et al. 2007). All elements in the TEDOR sequence were synchronized with the rotor frequency $\nu_r = 1/\tau_r$. For 1D and 2D TEDOR experiments, the t_{mix} was set to 1.28 ms ($16\times\tau_r$), which gave the maximum ^{13}Cα signal. The ^{15}N dwell time (t_1) was set to $4\times\tau_r$ (320 µs) during which a ^{1}H decoupling with 100 kHz RF amplitude was applied. The two Δ periods (z-filters) were set to 240 µs ($3\times\tau_r$) with ^{1}H RF set to 12.5 kHz to facilitate rapid dephasing of ^{13}C transverse magnetization (Jaroniec et al. 2002). Before and after t_1 evolution, a pair of 90° pulses with a total length of 24 µs were applied. To avoid desynchronization, an additional τ delay after t_1 evolution was set to 216 µs ($3\times\tau_r - 24$ µs) (Jaroniec et al. 2002; Hong and Griffin 1998). The pseudo-3D TEDOR-NCACX-NCOCX experiment was performed on U-^{13}C,^{15}N crystalline NAVL using 16 t_1 increments and a dwell time of 640 µs. The parameters for the 3D TEDOR experiments were similar to the 2D TEDOR with the t_{mix} period arrayed from 1.28 to 17.92 ms (Jaroniec et al. 2002). The 2D spectra of U-^{13}C,^{15}N SLN, U-^{13}C,^{15}N SatP, and U-^{13}C,^{15}N ubiquitin were acquired with 512, 400, and 128 scans, respectively. The pseudo-3D TEDOR-NCACX-NCOCX experiment on U-^{13}C,^{15}N NAVL was acquired using 64 scans. A ^{1}H RF amplitude of 12.5 kHz (ν_r) (Takegoshi and Terao 2001) was used for ^{13}C,^{13}C-DARR mixing periods.

Results

Simultaneous acquisition of TEDOR and NCX experiments

The original pulse sequence for the z-filtered (ZF) TEDOR experiment uses ^{1}H-^{13}C CP as a preparation period (Fig. 1A) (Jaroniec et al. 2002). In contrast, the new hybrid pulse sequence, TEDOR-NCX (Fig. 1B), starts with the SIM-CP sequence that creates both ^{13}C and ^{15}N polarization from the ^{1}H spin bath, which are utilized to record TEDOR and NCA (or NCO) experiments in the 1st and 2nd acquisition, respectively. The coherence transfer pathways for the hybrid TEDOR-NCX experiment can be described using the product operator formalism as follows:

$$
\begin{aligned}
&\sum H_z \xrightarrow{(90^{o}_{\varphi 1=y})^{H}-SIM\ CP} C_x + N_x \xrightarrow{(90^{o}_{-y})^{N}} C_x + N_z \\
&\xrightarrow{REDOR(t_{mix}/2)} C_x\cdot\cos(\omega\, t_{mix}/2) + 2C_yN_z\cdot\sin(\omega\, t_{mix}/2) + N_z \\
&\xrightarrow{(90^{o}_{x})^{C}-\Delta-(90^{o}_{\varphi*=y})^{N}} 2C_zN_x\cdot\sin(\omega\, t_{mix}/2) + N_x \\
&\xrightarrow{t_1-(90^{o}_{\varphi 2=-y})^{N}-\tau-(90^{o}_{x})^{C}} \left[-2C_yN_z\cdot\sin(\omega\, t_{mix}/2) + N_z\right]e^{i\omega_N t_1} \\
&\xrightarrow{REDOR(t_{mix}/2)} \left[-2C_yN_z\cdot\sin(\omega\, t_{mix}/2)\cdot\cos(\omega\, t_{mix}/2) + C_x\cdot\sin^2(\omega\, t_{mix}/2) + N_z\right]e^{i\omega_N t_1} \\
&\xrightarrow{(90^{o}_{-y})^{C}-\Delta-(90^{o}_{y})^{C}-t_2} \left[C_x\cdot\sin^2(\omega\, t_{mix}/2)\cdot e^{i\omega_N t_1}\cdot e^{i\omega_C t_2}\right]^{\text{TEDOR}}_{\text{1st Acquisiiton}} + N_z\cdot e^{i\omega_N t_1} \\
&\xrightarrow{(90^{o}_{y})^{N}-[SPECIFIC\ CP]^{NCA/NCO}} C_x\cdot e^{i\omega_N t_1} \xrightarrow{t_2} \left[C_x\cdot e^{i\omega_N t_1}\cdot e^{i\omega_C t_2}\right]^{NCA/NCO}_{\text{2nd Acquisiiton}}
\end{aligned}
\tag{1}
$$

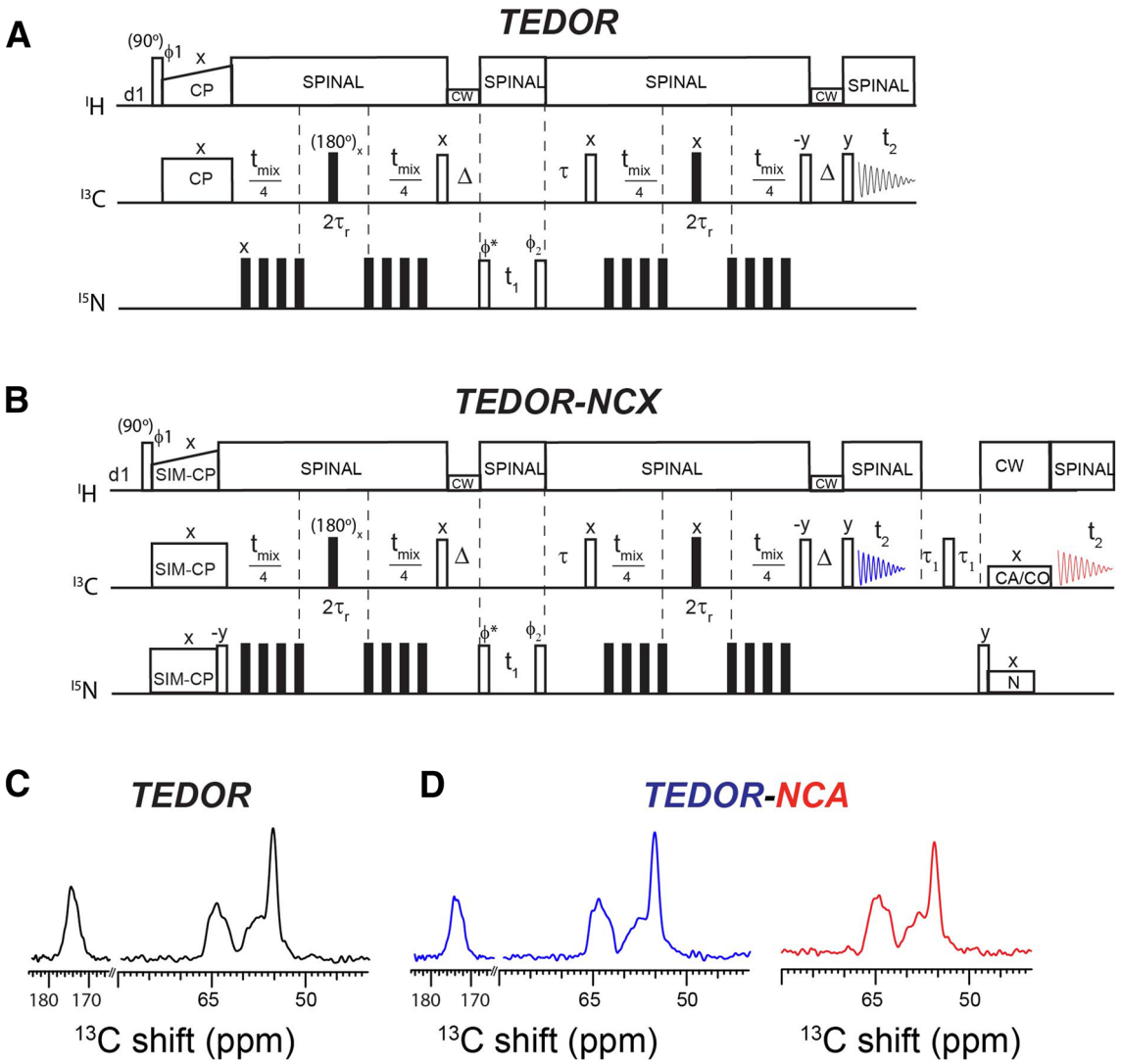

Fig. 1 **A** Pulse sequences for the conventional 2D Z-filtered TEDOR experiment. **B** Hybrid pulse sequence (TEDOR-NCX) that combines TEDOR and NCA (or NCO) experiments. **C** 1D spectrum of U-^{13}C,^{15}N SLN recorded using conventional TEDOR experiment (black). **D** 1D TEDOR and NCA spectra of U-^{13}C,^{15}N SLN acquired simultaneously with the TEDOR-NCA pulse sequence (blue and red). The phase cycles were ϕ_1 = y, − y, y, − y, ϕ_2 = y, y, − y, − y, and $\phi_{receiver}$ = y, − y, − y, y. XY-4 phase cycling scheme was applied for ^{15}N π pulses during TEDOR mixing periods. States mode detection of t_1 dimension was obtained by switching the ϕ* phase between y and − x

The ^{13}C and ^{15}N chemical shifts are represented by ω_C and ω_N, whereas ω represents the effective ^{13}C–^{15}N dipolar coupling. After SIM-CP, the ^{15}N polarization is stored along the z-axis (N_z) by applying a 90° pulse, whereas the ^{13}C transverse polarization is evolved through REDOR mixing ($t_{mix}/2$) to create an antiphase ^{13}C single quantum coherence ($2C_yN_z$). Note that the ^{15}N polarization remains along the z-axis after the 180° pulses are applied on the ^{15}N channel during the REDOR mixing period. The coherence transfer from ^{13}C to ^{15}N ($2C_zN_x$) is obtained by a pair of 90° pulses applied on both ^{13}C and ^{15}N channels, with the latter flipping N_z into the transverse spin operator N_X. Both in-phase and antiphase ^{15}N single-quantum operators (N_x and $2C_zN_x$) evolved simultaneously according to their chemical shifts during t_1 and under ^{1}H decoupling. The States quadrature detection in the t_1 dimension is achieved by switching the phase φ* of the ^{15}N pulse between y and − x prior to t_1 evolution. After t_1 evolution, a pair of 90° pulses is applied on ^{13}C and ^{15}N, which converts the antiphase operator $2C_zN_x$ into $2C_yN_z$ and the N_x operator into N_z. A τ period is used to compensate for rotor desynchronization caused by the duration of the 90° pulses. An identical REDOR mixing period ($t_{mix}/2$) converts the antiphase spin operator $2C_yN_z$ into the in-phase C_x operator, which gives rise to the TEDOR

signal detected during the 1st t_2 acquisition period. Note that in Eq. 1, the spin coherences such as $[C_x \cdot \cos(\omega \cdot t_{mix}/2)]$, $[2C_yN_z \cdot \sin(\omega \cdot t_{mix}/2) \cdot \cos(\omega \cdot t_{mix}/2)]$, and other multiple quantum terms (not shown) created by homonuclear ^{13}C–^{13}C *J*-couplings are eliminated by ^{15}N phase cycling (φ_2) and Δ periods as shown in Fig. 1A, B (Jaroniec et al. 2002). The TEDOR mixing period t_{mix} (Eq. 1, and Fig. 1) can be adjusted to optimize the ^{15}N–^{13}C transfer. For example, one bond ^{15}N–^{13}C transfer requires up to 1.2 ms mixing period. After this first acquisition, a τ_1-90°-τ_1 sequence ($\tau_1 = 3$ ms) is applied on the ^{13}C channel to remove any residual ^{13}C magnetization (Gopinath and Veglia 2012a, b). The N_z is then tilted into the transverse plane by a 90° pulse followed by a SPECIFIC-CP transfer from ^{15}N to $^{13}C\alpha$ or ^{15}N to ^{13}CO, which is detected in the second acquisition period (t_2).

Figure 1C, D show 1D TEDOR and NCA spectra of U-^{13}C,^{15}N SLN obtained from TEDOR and the hybrid TEDOR-NCA pulse sequences. These spectra were obtained by setting the t_1 evolution period to zero and using a mixing time (t_{mix}) of 1.28 ms. The integrated intensities were normalized to the corresponding intensities of the TEDOR spectrum to determine possible signal losses. For the $^{13}C\alpha$ region (50–70 ppm), we obtained integrated signal intensities of 1.00 and 0.99 using conventional TEDOR and TEDOR-NCA sequences, respectively, whereas the corresponding values for the ^{13}CO region (165–180 ppm) were 1.00 and 0.94. The marginal loss of ^{13}CO signal intensity detected for the TEDOR-NCA pulse sequence is due to the SIM-CP transfer implemented in the preparation period, which usually reduces the intensity of the ^{13}CO signals by 5–10% (Gopinath and Veglia 2012a, b). Figure 1D also shows the 1D NCA spectrum from the 2nd acquisition of the TEDOR-NCA experiment. In this case, the normalized integrated intensities of $^{13}C\alpha$ region from TEDOR (1st acquisition) and NCA (2nd acquisition) were 1.00 and 0.95, respectively. Note that these two spectra can be added to increase the S/N ratio by 38%.

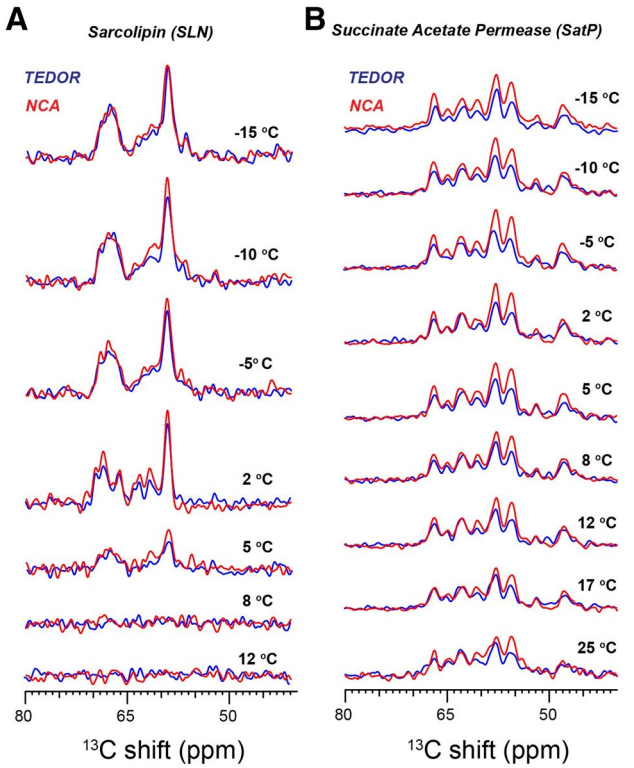

Fig. 2 Temperature dependence of the $^{13}C\alpha$ signal intensities of 1D TEDOR and NCA spectra of **A** single transmembrane protein U-^{13}C,^{15}N SLN, and **B** six transmembrane U-^{13}C,^{15}N SatP. All spectra were acquired using TEDOR-NCA pulse sequence reported in Fig. 1B

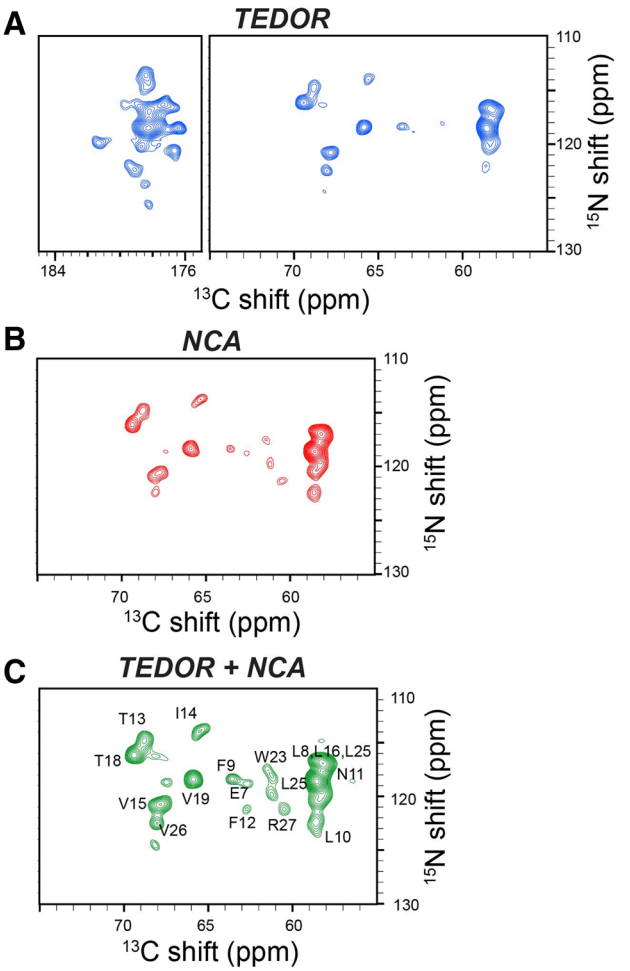

Fig. 3 **A** 2D TEDOR spectrum of SLN (blue); **B** 2D NCA spectrum of SLN (red). Both A and B were acquired simultaneously using the TEDOR-NCA pulse sequence. **C** Sum of the TEDOR and NCA spectra. The resonances in the spectrum have an average sensitivity enhancement of 32% for $^{13}C\alpha$ region. All the spectra were plotted at same noise level

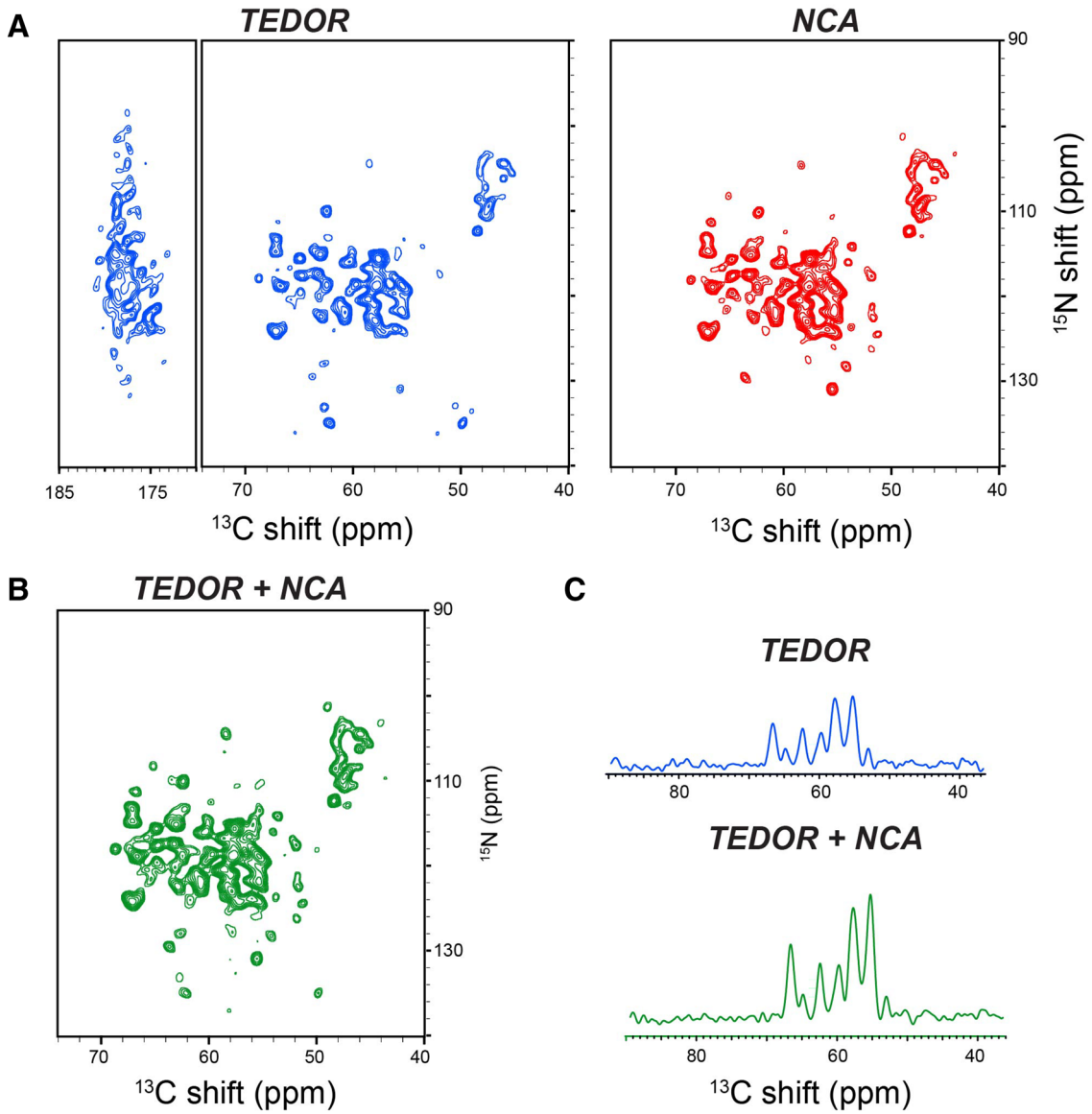

Fig. 4 **A** 2D TEDOR and NCA spectra of SatP acquired simultaneously using the TEDOR-NCA pulse sequence. **B** Sum of the 2D TEDOR and NCA spectra showing an average sensitivity enhancement of 60% for ^{13}Cα region with respect to the conventional TEDOR experiment. All the 2D spectra were plotted at same noise level. **C** 1D cross sections of TEDOR and TEDOR + NCA spectra along ^{15}N dimension at 119 ppm, showing the signal enhancement

To understand the effects of temperature on ^{13}C signal intensities, we acquired a series of 1D TEDOR and NCA spectra of U-^{13}C,^{15}N SLN and U-^{13}C,^{15}N SatP at temperatures above and below the phase transition of the DMPC lipid bilayer (Fig. 2). For U-^{13}C,^{15}N SatP, the integrated intensities of 1D NCA spectra (red) are about 10–30% higher than the corresponding TEDOR spectra (blue). In contrast, the intensities of the TEDOR and NCA spectra performed on U-^{13}C,^{15}N SLN are virtually identical. The highest peak intensities and resolution for both proteins were obtained at 2 °C, where DMPC is in the gel phase. The signal intensities for both samples gradually decrease upon reaching DMPC's liquid crystalline phase (i.e., 20–30 °C), with signal intensities of both TEDOR and NCA spectra following similar trends.

A comparison of the 2D TEDOR-NCA experiments on U-^{13}C,^{15}N SLN and U-^{13}C,^{15}N SatP are reported in Figs. 3 and 4. Specifically, Fig. 3A, B show 2D TEDOR-NCA spectra of U-^{13}C,^{15}N SLN. After summing the TEDOR and NCA data sets, we obtained an average net increase in signal intensity of 32% (Fig. 3C). Note that the sum of the two spectra also increases the noise level by $\sqrt{2}$, therefore intensities were scaled down by a factor of 0.707 ($1/\sqrt{2}$) when quantifying signal in the spectrum

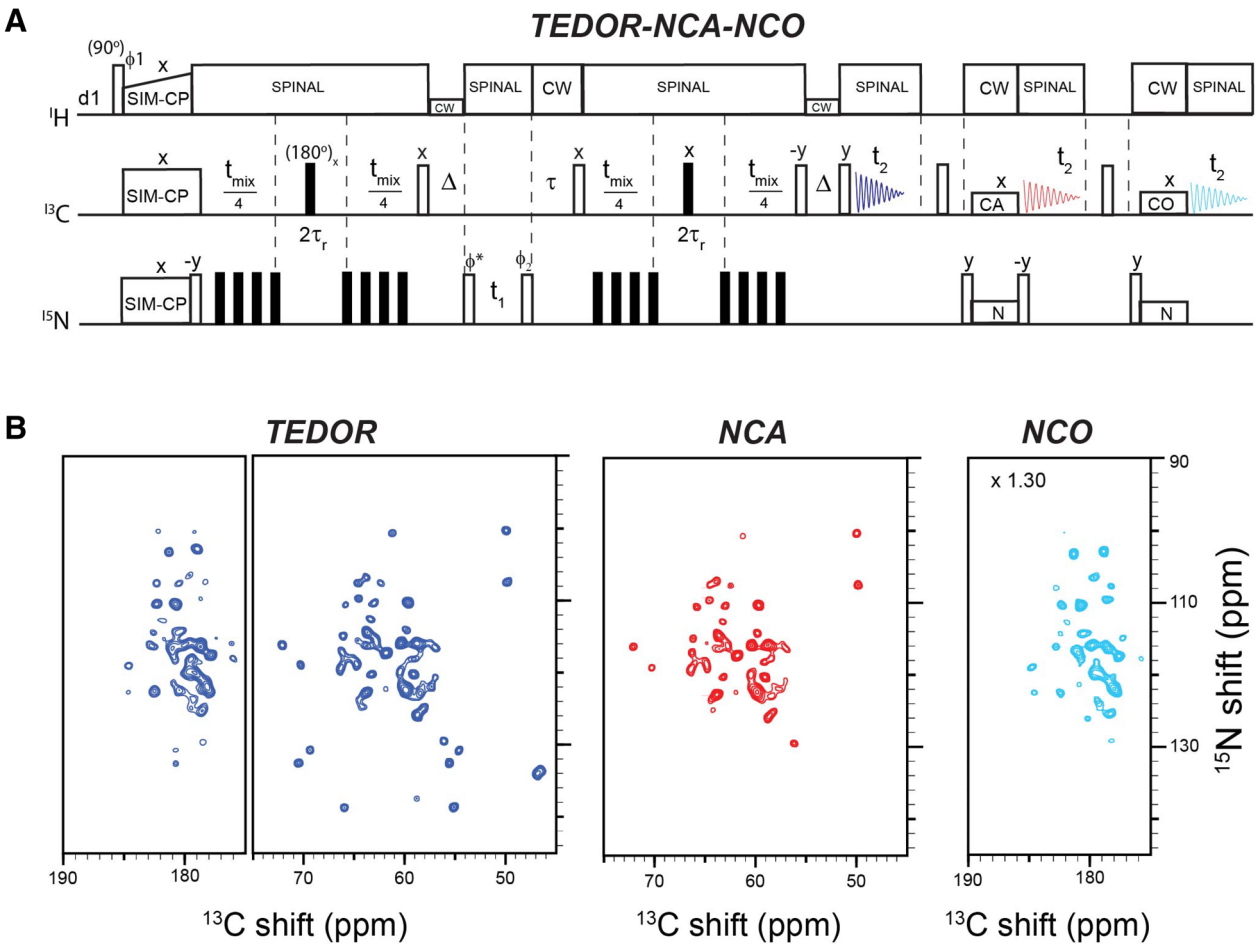

Fig. 5 **A** TEDOR-NCA-NCO pulse sequence for simultaneous acquisition of TEDOR, NCA and NCO experiments. **B** Spectra of U-^{13}C–^{15}N ubiquitin microcrystalline sample recorded with the pulse sequence in **A**. The 2D spectra of TEDOR and NCA were drawn at same noise level, whereas NCO spectrum was multiplied by 1.30 to show all the resonances

of Fig. 3C. The peak positions of U-^{13}C,^{15}N SLN match our previous resonance assignments obtained with the 3D-DUMAS-NCACX-CANCO experiment (Gopinath and Veglia 2012; Mote et al. 2013). The total time for acquiring 2D TEDOR-NCA spectra was 27.8 h and the additional 2nd acquisition increased the experimental time by only 16 min. In contrast, to record only a single spectrum with the conventional 2D TEDOR experiment would have taken 27.5 h. We repeated the 2D TEDOR-NCA experiment for U-^{13}C,^{15}N SatP (Fig. 4A). SatP is a significantly larger membrane protein, with six transmembrane domains arranged in ordered hexamers in the lipid membrane. The relative intensity of the 2D NCA for the ^{13}C (40–70 ppm) and ^{15}N (100–140 ppm) spectral regions is ~ 30% higher than the TEDOR spectrum. The sum of TEDOR and NCA spectra obtained has a signal intensity gain of 60% with respect to the TEDOR spectrum alone (Fig. 4A). This intensity gain is apparent in Fig. 4C, where 1D cross sections taken at 119 ppm of the ^{15}N dimension are reported for TEDOR and TEDOR + NCA spectra.

Simultaneous acquisition of TEDOR, NCA, and NCO correlation experiments

The hybridization of TEDOR and SPECIFIC-CP enables the concatenation of TEDOR, NCA, and NCO experiments for their simultaneous detection (Fig. 5A). The pulse sequence is an extension of 2D TEDOR-NCA and utilizes the residual ^{15}N polarization stored on the z-axis by a 90° pulse after NCA transfer. The first and second acquisitions enable the recording of TEDOR and NCA spectra, respectively. After the second acquisition, the residual ^{15}N polarization ('orphan' or 'afterglow' polarization) (Gopinath and Veglia 2013; Banigan and Traaseth 2012) is transferred to ^{13}CO by a 90° pulse and the NCO transfer using SPECIFIC-CP, which creates an NCO correlation experiment recorded in the third acquisition period. As shown previously, 30–35%

A

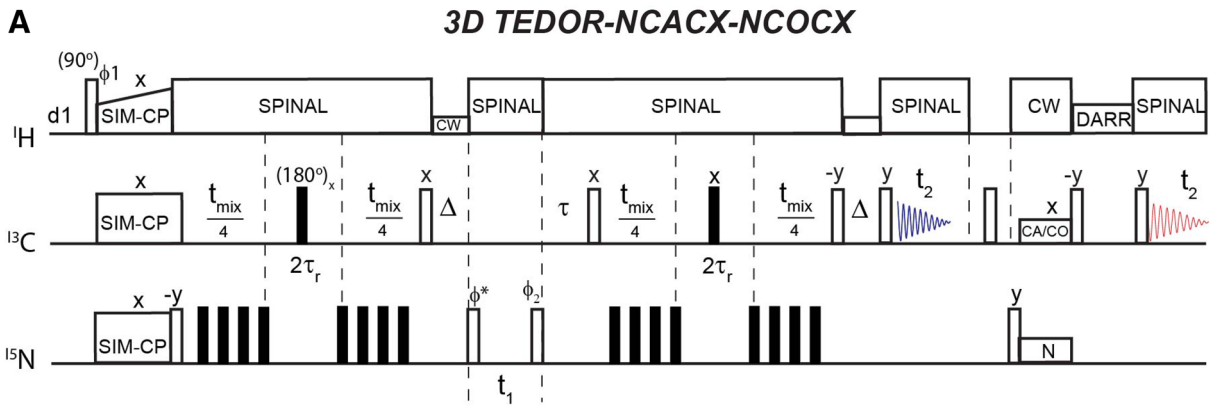

B

3D-TEDOR t_{mix} (ms)	2D NCACX (DARR mixing ms)	3D-TEDOR t_{mix} (ms)	2D NCOCX (DARR mixing ms)
1.280	NCA	10.240	NCO
2.560	NCACX (10)	11.520	NCOCX (10)
3.840	NCACX (50)	12.800	NCOCX (50)
5.120	NCACX (100)	14.080	NCOCX (100)
6.400	NCACX (150)	15.360	NCOCX (150)
7.680	NCACX (200)	16.640	NCOCX (200)
8.960	NCACX (300)	17.920	NCOCX (300)

Fig. 6 **A** Hybrid pulse sequence for simultaneous acquisition of 3D TEDOR, NCACX, and NCOCX experiments. **B** Table reporting the different mixing times for TEDOR and DARR used for the experiments on the NAVL peptide (see also Fig. 7)

of signal intensity is retained by the residual ^{15}N polarization after the NCA transfer (Gopinath and Veglia 2013; Banigan and Traaseth 2012), hence the third spectrum is typically 30–35% less intense than the second spectrum. To demonstrate the performance of the hybridized TEDOR-NCA-NCO pulse sequence, we used a U-^{13}C,^{15}N microcrystalline ubiquitin sample (Fig. 5B). The integrated intensities of 2D NCA and NCO spectra (red and green, respectively) are 1.2 and 0.7 times, respectively, that of the TEDOR spectrum (blue). As shown in Figs. 4 and 5 for both U-^{13}C,^{15}N SatP and U-^{13}C,^{15}N ubiquitin, TEDOR-NCA, TEDOR-NCO or TEDOR-NCA-NCO experiments offer an efficient way to assign Pro resonances. In fact, Pro resonances, which are typically located between 128 and 135 ppm in the^{15}N dimension, display substantially higher signals in the TEDOR spectra compared to NCA spectra. This is due to inefficient ^{15}N CP caused by the absence of directly bound protons to the imino groups of Pro residues. In contrast, TEDOR detects Pro residues more efficiently by using ^{13}C CP followed by a CANCA or CONCO pathway.

Simultaneous acquisition of 3D-TEDOR, NCACX, and NCOCX experiments

Using a similar strategy, we hybridized 3D TEDOR, NCACX, and NCOCX experiments (Fig. 6). In this pulse sequence, a 3D TEDOR spectrum is acquired during the first acquisition, whereas NCACX and NCOCX are recorded in the second acquisition. Typically, 3D TEDOR requires 12 to 18 mixing periods, which can be synchronized with NCACX and NCOCX experiments having different DARR mixing times. Figure 6B, shows a table with 14 mixing times for the 3D TEDOR experiment in the first acquisition. For the second acquisition, the 3D TEDOR experiment is synchronized with seven NCACX and seven NCOCX experiments, with DARR mixing times set to 0, 10, 50, 100,150, 200, and 300 ms. As a benchmark, we used U-^{13}C,^{15}N *N*-acetyl-Valine-Leucine (NAVL) dipeptide with an unlabeled acetyl group. Figure 7A, B show the strip plots extracted from the 3D-TEDOR, NCACX and NCOCX spectra of NAVL. The corresponding intensities of the TEDOR cross peaks

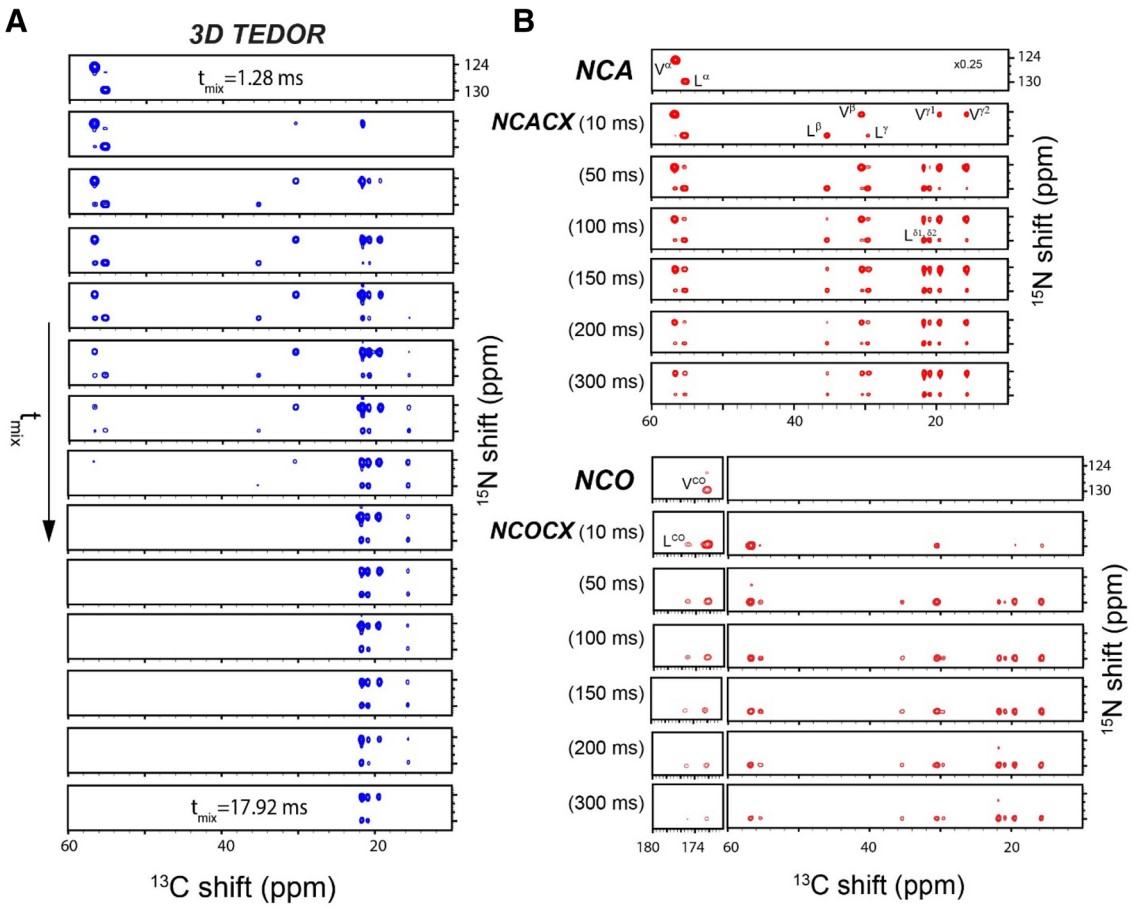

Fig. 7 3D spectra of NAVL dipeptide acquired simultaneously with the TEDOR-NCACX-NCOCX pulse sequence. **A** TEDOR spectra at different mixing times. **B** NCACX, and NCOCX spectra at different DARR mixing times

observed between Val N to Val Cβ, and Leu N to Val Cβ as a function of the mixing time are reported in Fig. 8A. Even at short mixing times, the signal-to-noise ratio for the cross-peaks is greater than 15 and the resulting experimental error bars are contained within the symbols. The peak intensities were fit to simulated curves using the equations reported in reference (Jaroniec et al. 2002), where the intra-residue distance between Val N to Val Cβ was set to 2.7 Å, and the inter-residue distance between Leu N to Val Cβ was set to 3.5 Å. These distances are in close agreement with those reported in the literature (Jaroniec et al. 2002). Note that the NAVL crystal used in this work contains 100% U-^{13}C,^{15}N labeled molecules, which may cause slight deviations from the theoretical TEDOR curves due to inter-molecular dipolar couplings. Figure 8B shows the plot of the intensities of ^{13}C–^{13}C cross-peaks between Val Cα to Val Cβ and Val Cα to Leu Cα obtained from the NCACX spectra at various DARR mixing times (Fig. 7B). The peak intensities were normalized with the Val Cα peak of the NCA spectrum (Fig. 7B). As expected, the Val Cα-Cβ cross peak has the highest intensity at shorter DARR mixing time (50 ms). On the other hand, the inter-residue cross peak between Val Cα to Leu Cα requires 150 ms DARR mixing time to build up completely and reaches a plateau due to spin diffusion. Note that in general the DARR peak intensities are less quantitative than TEDOR experiments; therefore, it is advisable to acquire multiple DARR spectra at different mixing times and classify peak intensities as short-, medium-, and long-range distances of up to 10 Å (Zhang et al. 2010; Ekanayake et al. 2016). Note that in the 3D experiment, the initial polarization of NCACX and NCOCX experiments can be slightly different due to the effect of 180° pulses on ^{15}N z-magnetization during the TEDOR mixing. Figure 9 shows the intensity variation of 1D NCA spectra of NAVL sample acquired in the second acquisition at different TEDOR mixing times. Even at longer mixing times (10–15 ms), the loss of intensity is less than 10% with respect to the initial mixing period of 1.28 ms.

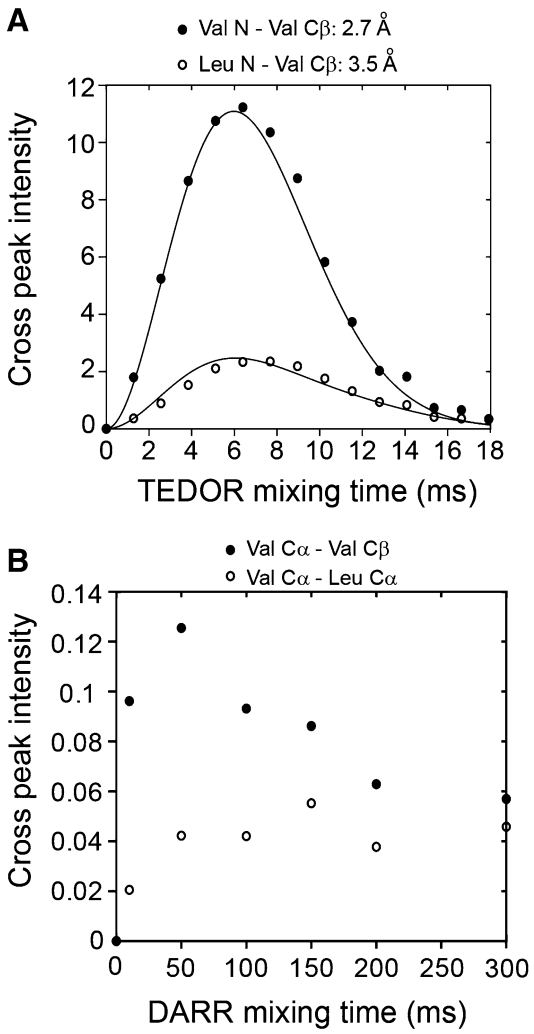

Fig. 8 Simultaneous measurement of ^{15}N-^{13}C and ^{13}C-^{13}C distance restraints on NAVL dipeptide from 3D-TEDOR-NCACX-NCOCX spectra of Fig. 7. **A** 3D TEDOR cross peak intensities as a function of the mixing time. The Val N to Val Cβ cross peaks are indicated as filled circles. The cross peaks for Leu N to Val Cβ are indicated with open circles. The cross peak intensities were fit with simulated curves using 2.7 and 3.5 Å, respectively. **B** NCACX cross peak intensities between Val Cα–Cβ and Val Cα–Leu Cα plotted at different DARR mixing times

Discussion

In ssNMR, the efficiency of CP transfer periods is often compromised by ^{1}H–^{1}H spin diffusion. As a result, only a portion of nuclear polarization generated in the preparation periods is converted into observable coherences. Pines and Waugh were the first to exploit the residual polarization of the rich ^{1}H spin bath to acquire multiple ^{1}H-enhanced CP spectra and increase the signal-to-noise ratio of solid samples (Pines et al. 1972). More recently, Tang and Nevzorov proposed a comparable scheme to enhance the sensitivity of oriented membrane protein samples (Tang and Nevzorov 2011). In spite of that, most pulse sequences are inefficient and many spin operators remain essentially undetectable (orphan spin operators) (Gopinath et al. 2016, 2011; Gopinath and Veglia 2009).

During the past decade, our group has developed POEs to recover orphan spin operators for signal enhancements or acquire multiple spectra from single pulse sequences in both oriented and MAS ssNMR (Gopinath and Veglia 2009, 2012a, b, 2013, 2016; Gopinath et al. 2011, 2016). POE experiments in MAS are based on the SIM-CP preparation period, where the rich ^{1}H spin bath enables the simultaneous generation of ^{13}C and ^{15}N polarization pathways, which are then utilized for acquiring 2D multidimensional experiments using DUMAS pulse sequences (Gopinath and Veglia 2012a, b; Gopinath et al. 2016). In addition, POE utilizes ^{13}C and ^{15}N residual polarization pathways resulting from N–C CP periods and generates four to eight multi-dimensional spectra (MEIOSIS and MAESTOSO-8) (Gopinath and Veglia 2013, 2016). Other groups have paralleled our efforts. For instance, the use of ^{15}N residual polarization pathways have also been utilized by Ramachandran and co-workers for acquiring multiple experiments under fast MAS conditions (Bellstedt et al. 2012). Similarly, the 'afterglow' pulse sequences developed by the Traaseth lab exploits the residual ^{15}N polarization and simultaneously records NCA and NCO spectra (Banigan and Traaseth 2012). The afterglow phenomenon has been used in concert with SIM-CP for the MEOSIS scheme to record four 2D spectra simultaneously [DARR, NCACX, NCO and CA(N)CO] (Gopinath and Veglia 2013).

Our previously published POEs were able to generate a ^{13}C–^{13}C homonuclear correlated spectrum in the first acquisition and exploit the additional ^{15}N or ^{13}C polarization for single or multiple ^{13}C–^{13}C and ^{13}C–^{15}N correlation experiments (Gopinath and Veglia 2012a, b, 2015, 2016). By hybridizing TEDOR and NCX experiments in this work, we introduced a novel way to obtain multiple ^{15}N–^{13}C experiments for both resonance assignments and distance measurements. This new sub-class of POEs takes advantage of the small dipolar couplings (~ 1 kHz) associated with NCA or NCO spin pairs that enable the ^{15}N–^{13}C polarization transfer. In the original TEDOR pulse sequence, the ^{15}N–^{13}C dipolar recoupling is achieved by using a pair of REDOR mixing periods (Jaroniec et al. 2002; Hing and Schaefer 1993); whereas the NCX (NCA or NCO) transfer uses a selective ^{15}N–^{13}C recoupling via Hartmann-Hahn matching using SPECIFIC-CP (Baldus et al. 1998; Hartmann and Hahn 1962). A key difference between TEDOR and NCX experiments is the initial preparation period. While TEDOR uses the ^{13}C polarization originating from ^{1}H–^{13}C CP, the NCX experiment uses the ^{15}N polarization from ^{1}H–^{15}N CP. The hybridized 2D and 3D TEDOR-NCX pulse sequences combine these two pathways for generating multiple ^{15}N–^{13}C correlation spectra.

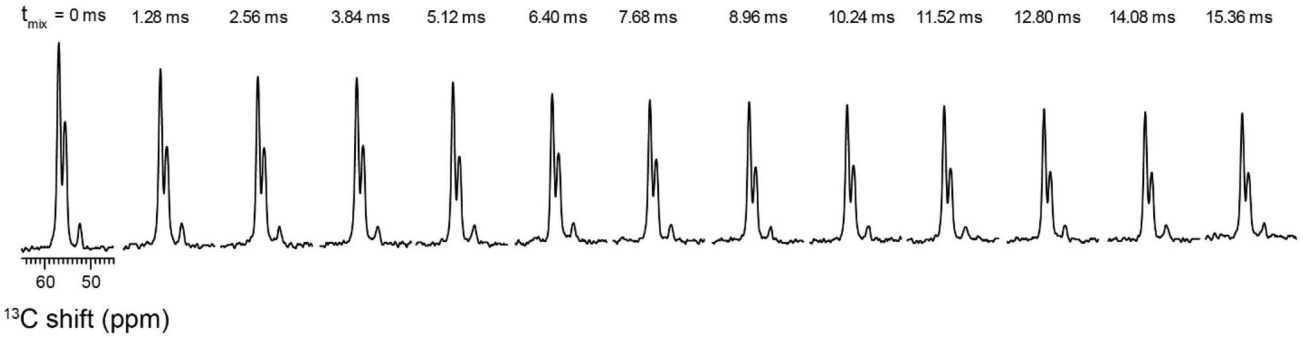

Fig. 9 Effects of the TEDOR 180° pulses on the ^{15}N z-magnetization of the NAVL dipeptide as monitored by 1D NCA spectra. The spectra refer to the second acquisition of the pulse sequence reported in Fig. 6A

The optimal performance of TEDOR and SPECIFIC-CP depends on the sample characteristics as well as quality of the NMR hardware (RF homogeneity and probes). For instance, longer transfer periods for SPECIFIC-CP (3–6 ms) may cause inefficient polarization transfer due to fast $T_{1\rho}$ relaxation and/or RF inhomogeneity (Jain et al. 2012; Daviso et al. 2013). In the most favorable cases, the latter problem can be overcome by using shaped pulses to suppress RF inhomogeneity during the NC transfer (Jain et al. 2012; Tosner et al. 2018; Manu and Veglia 2016). Note also that TEDOR transfer relies on the efficiency of 180° pulses and T_2 relaxation of the antiphase spin operators, which is relatively short for biomolecular solids. A detailed description of how RF inhomogeneity and sample characteristics affect the ssNMR experiments can be found in the references (Paulson et al. 2004; Tosner et al. 2017; Tekely and Goldman 2001). In our hands, however, we found that NCA transfer is more efficient than TEDOR for membrane proteins such as SatP (Figs. 2, 4). Therefore, the performance of these two techniques may depend mostly on sample heterogeneity and protein dynamics. In fact, the RF inhomogeneity compensated shaped pulses can also be applied to hybrid TEDOR-NCX pulse sequences. From a technical viewpoint, the application of POEs with multiple acquisitions may result in an increase of RF duty cycles; however, the pulse sequences designed here are within the power limits indicated for the commercially available E-free or low-E MAS ssNMR probes (Gor'kov et al. 2007; McNeill et al. 2009; Stringer et al. 2005).

In recent years, several different techniques have been proposed to speed up the acquisition of MAS ssNMR experiments. Among those, the conjoined ultra-fast MAS with proton detection (Zhang et al. 2017; Andreas et al. 2015; Demers et al. 2011; Zhou et al. 2007; Struppe et al. 2017; Wang et al. 2015) and sparse protein perdeuteration (Reif 2012) have produced spectra with the resolution and sensitivity comparable to those of liquid-state NMR. Additionally, Ishii and co-workers introduced the use of paramagnetic relaxation agents, reducing recycle delays and increasing the repetition times (Wickramasinghe et al. 2009). However, the most significant sensitivity enhancement for biomolecular solids has been achieved using dynamic nuclear polarization (DNP) (Barnes et al. 2008), with recent applications on several biological macromolecules. The pulse sequences presented here can be implemented with the above techniques in a synergistic way to boost even more the sensitivity and resolution of multidimensional NMR experiments for biomolecular samples.

Conclusions

In conclusion, we introduced a new sub-class of POE pulse sequences for simultaneous acquisition of multiple NC correlation spectra using a single receiver. Both 2D and 3D TEDOR experiments are combined with NC or NCC sequences for recording ^{15}N–^{13}C fingerprints as well as simultaneous measurements of ^{15}N–^{13}C and ^{13}C–^{13}C distances. These experiments are not alternatives to the existing approaches for sensitivity enhancement; rather they provide novel strategies that can be combined with the current methods to speed up data acquisition and lead to faster structure determination of proteins in different folded states.

Acknowledgements This work was supported by the National Institute of Health (GM 64742 to G.V. and R35 GM118047 to H.A.). Many thanks to Dr. D. Weber for critical reading and editing the manuscript.

References

Ader C et al (2009) Structural rearrangements of membrane proteins probed by water-edited solid-state NMR spectroscopy. J Am Chem Soc 131:170–176

Andreas LB, Le Marchand T, Jaudzems K, Pintacuda G (2015) High-resolution proton-detected NMR of proteins at very fast MAS. J Magn Reson 253:36–49

Andrew W, Hing S, Schaefer J (1992) Transferred-echo double-resonance NMR. J Magn Reson 96:205–209
Baldus M, Petkova AT, Herzfeld J, Griffin RG (1998) Cross polarization in the tilted frame: assignment and spectral simplification in heteronuclear spin systems. Mol Phys 95:1197–1207
Banigan JR, Traaseth NJ (2012) Utilizing afterglow magnetization from cross-polarization magic-angle-spinning solid-state NMR spectroscopy to obtain simultaneous heteronuclear multidimensional spectra. J Phys Chem B 116:7138–7144
Barnes AB et al (2008) High-field dynamic nuclear polarization for solid and solution biological NMR. Appl Magn Reson 34:237–263
Bellstedt P et al (2012) Solid state NMR of proteins at high MAS frequencies: symmetry-based mixing and simultaneous acquisition of chemical shift correlation spectra. J Biomol NMR 54:325–335
Buck B et al (2003) Overexpression, purification, and characterization of recombinant Ca-ATPase regulators for high-resolution solution and solid-state NMR studies. Protein Expr Purif 30:253–261
Castellani F et al (2002) Structure of a protein determined by solid-state magic-angle-spinning NMR spectroscopy. Nature 420:98–102
Das BB, Opella SJ (2016) Simultaneous cross polarization to (13)C and (15)N with (1)H detection at 60 kHz MAS solid-state NMR. J Magn Reson 262:20–26
Daviso E, Eddy MT, Andreas LB, Griffin RG, Herzfeld J (2013) Efficient resonance assignment of proteins in MAS NMR by simultaneous intra- and inter-residue 3D correlation spectroscopy. J Biomol NMR 55:257–265
Demers JP, Chevelkov V, Lange A (2011) Progress in correlation spectroscopy at ultra-fast magic-angle spinning: Basic building blocks and complex experiments for the study of protein structure and dynamics. Solid State Nucl Magn Reson 40:101–113
Ekanayake EV, Fu R, Cross TA (2016) Structural influences: cholesterol, drug, and proton binding to full-length influenza A M2 protein. Biophys J 110:1391–1399
Franks WT, Kloepper KD, Wylie BJ, Rienstra CM (2007) Four-dimensional heteronuclear correlation experiments for chemical shift assignment of solid proteins. J Biomol NMR 39:107–131
Fung BM, Khitrin AK, Ermolaev K (2000) An improved broadband decoupling sequence for liquid crystals and solids. J Magn Reson 142:97–101
Gopinath T, Veglia G (2009) Sensitivity enhancement in static solid-state NMR experiments via single- and multiple-quantum dipolar coherences. J Am Chem Soc 131:5754–5756
Gopinath T, Veglia G (2012a) Dual acquisition magic-angle spinning solid-state NMR-spectroscopy: simultaneous acquisition of multidimensional spectra of biomacromolecules. Angew Chem Int Ed Engl 51:2731–2735
Gopinath T, Veglia G (2012b) 3D DUMAS: simultaneous acquisition of three-dimensional magic angle spinning solid-state NMR experiments of proteins. J Magn Reson 220:79–84
Gopinath T, Veglia G (2013) Orphan spin operators enable the acquisition of multiple 2D and 3D magic angle spinning solid-state NMR spectra. J Chem Phys 138:184201
Gopinath T, Veglia G (2015) Multiple acquisition of magic angle spinning solid-state NMR experiments using one receiver: application to microcrystalline and membrane protein preparations. J Magn Reson 253:143–153
Gopinath T, Veglia G (2016a) Multiple acquisitions via sequential transfer of orphan spin polarization (MAeSTOSO): How far can we push residual spin polarization in solid-state NMR? J Magn Reson 267:1–8
Gopinath T, Veglia G (2016b) Orphan spin polarization: A catalyst for high-throughput solid-state NMR spectroscopy of proteins. Ann Rep NMR Spectrosc 89:103–121
Gopinath T, Veglia G (2018) Experimental aspects of polarization optimized experiments (POE) for magic angle spinning solid-state NMR of microcrystalline and membrane-bound proteins. Methods Mol Biol 1688:37–53
Gopinath T, Mote KR, Veglia G (2011) Proton evolved local field solid-state nuclear magnetic resonance using Hadamard encoding: theory and application to membrane proteins. J Chem Phys 135:074503
Gor'kov PL et al (2007) Using low-E resonators to reduce RF heating in biological samples for static solid-state NMR up to 900 MHz. J Magn Reson 185:77–93
Gullion T, Schaefer J (1989) Development of REDOR rotational-echo double-resonance NMR. J Magn Reson 81:196
Gullion T, Baker DB, Conradi MS (1990) New, compensated Carr-Purcell sequences. J Magn Reson 89:479–484
Gustavsson M et al (2013) Allosteric regulation of SERCA by phosphorylation-mediated conformational shift of phospholamban. Proc Natl Acad Sci USA 110:17338–17343
Hartmann SR, Hahn EL (1962) Nuclear double resonance in the rotating frame. Phys Rev 128:2042–2053
Hing AW, Schaefer J (1993) Two-dimensional rotational-echo double resonance of Val1-[1-13C]Gly2-[15N]Ala3-gramicidin A in multilamellar dimyristoylphosphatidylcholine dispersions. Biochemistry 32:7593–7604
Hong M, Griffin RG (1998) Resonance assignments for solid peptides by dipolar-mediated C-13/N-15 correlation solid-state NMR. J Am Chem Soc 120:7113–7114
Hong M, Zhang Y, Hu F (2012) Membrane protein structure and dynamics from NMR spectroscopy. Annu Rev Phys Chem 63:1–24
Hu F, Luo W, Hong M (2010) Mechanisms of proton conduction and gating in influenza M2 proton channels from solid-state NMR. Science 330:505–508
Igumenova TI et al (2004) Assignments of carbon NMR resonances for microcrystalline ubiquitin. J Am Chem Soc 126:6720–6727
Jain S, Bjerring M, Nielsen NC (2012) Efficient and robust heteronuclear cross-polarization for high-speed-spinning biological solid-state NMR spectroscopy. J Phys Chem Lett 3:703–708
Jaroniec CP, Filip C, Griffin RG (2002) 3D TEDOR NMR experiments for the simultaneous measurement of multiple carbon–nitrogen distances in uniformly (13)C,(15)N-labeled solids. J Am Chem Soc 124:10728–10742
Manu VS, Veglia G (2016) Optimization of identity operation in NMR spectroscopy via genetic algorithm: application to the TEDOR experiment. J Magn Reson 273:40–46
McNeill SA, Gor'kov PL, Shetty K, Brey WW, Long JR (2009) A low-E magic angle spinning probe for biological solid state NMR at 750 MHz. J Magn Reson 197:135–144
Mote KR, Gopinath T, Veglia G (2013) Determination of structural topology of a membrane protein in lipid bilayers using polarization optimized experiments (POE) for static and MAS solid state NMR spectroscopy. J Biomol NMR 57:91–102
Paulson EK, Martin RW, Zilm KW (2004) Cross polarization, radio frequency field homogeneity, and circuit balancing in high field solid state NMR probes. J Magn Reson 171:314–323
Pines A, Waugh JS, Gibby MG (1972) Proton-enhanced nuclear induction spectroscopy—method for high-resolution NMR of dilute spins in solids. J Chem Phys 56:1776
Qiu B et al (2018) Succinate–acetate permease from *Citrobacter koseri* is an anion channel that unidirectionally translocates acetate. Cell Res 28:644–654
Reif B (2012) Ultra-high resolution in MAS solid-state NMR of perdeuterated proteins: implications for structure and dynamics. J Magn Reson 216:1–12
Rienstra CM et al (2002) De novo determination of peptide structure with solid-state magic-angle spinning NMR spectroscopy. Proc Natl Acad Sci USA 99:10260–10265

Sa-Pessoa J et al (2013) SATP (YaaH), a succinate–acetate transporter protein in *Escherichia coli*. Biochem J 454:585–595

Sharma K, Madhu PK, Mote KR (2016) A suite of pulse sequences based on multiple sequential acquisitions at one and two radiofrequency channels for solid-state magic-angle spinning NMR studies of proteins. J Biomol NMR 65:127–141

Stringer JA et al (2005) Reduction of RF-induced sample heating with a scroll coil resonator structure for solid-state NMR probes. J Magn Reson 173:40–48

Struppe J et al (2017) Expanding the horizons for structural analysis of fully protonated protein assemblies by NMR spectroscopy at MAS frequencies above 100 kHz. Solid State Nucl Magn Reson 87:117–125

Sun P et al. (2018) Crystal structure of the bacterial acetate transporter SatP reveals that it forms a hexameric channel. J Biol Chem 293:19492–19500

Takegoshi KN, S; and Terao T (2001) 13C–1H dipolar-assisted rotational resonance in magic-angle spinning NMR. Chem Phys Lett 344:631–637

Tang W, Nevzorov AA (2011) Repetitive cross-polarization contacts via equilibration-re-equilibration of the proton bath: sensitivity enhancement for NMR of membrane proteins reconstituted in magnetically aligned bicelles. J Magn Reson 212:245–248

Tekely P, Goldman M (2001) Radial-field sidebands in MAS. J Magn Reson 148:135–141

Tosner Z et al (2017) Radiofrequency fields in MAS solid state NMR probes. J Magn Reson 284:20–32

Tosner Z et al (2018) Overcoming volume selectivity of dipolar recoupling in biological solid-state NMR spectroscopy. Angew Chem Int Ed Engl 57:14514–14518

Traaseth NJ et al (2008) Structural and dynamic basis of phospholamban and sarcolipin inhibition of Ca(2+)-ATPase. Biochemistry 47:3–13

Wang S, Ladizhansky V (2014) Recent advances in magic angle spinning solid state NMR of membrane proteins. Prog Nucl Magn Reson Spectrosc 82C:1–26

Wang S et al (2015) Nano-mole scale sequential signal assignment by (1)H-detected protein solid-state NMR. Chem Commun 51:15055–15058

Wickramasinghe NP et al (2009) Nanomole-scale protein solid-state NMR by breaking intrinsic 1HT1 boundaries. Nat Methods 6:215–218

Zhang Y et al (2010) Resonance assignment and three-dimensional structure determination of a human alpha-defensin, HNP-1, by solid-state NMR. J Mol Biol 397:408–422

Zhang R, Mroue KH, Ramamoorthy A (2017) Proton-based ultrafast magic angle spinning solid-state NMR spectroscopy. Acc Chem Res 50:1105–1113

Zhou DH et al (2007) Proton-detected solid-state nmr spectroscopy of fully protonated proteins at 40 kHz magic-angle spinning. J Am Chem Soc 129:11791–11801